Acta Materialia 122 (2017) 199–206

Contents lists available at ScienceDirect

Acta Materialia

journal homepage: www.elsevier.com/locate/actamat

Full length article

The effects of prior austenite grain boundaries and microstructural morphology on the impact toughness of intercritically annealed medium Mn steel

Jeongho Han [a, b], Alisson Kwiatkowski da Silva [a], Dirk Ponge [a, *], Dierk Raabe [a], Sang-Min Lee [c], Young-Kook Lee [c, **], Sang-In Lee [d], Byoungchul Hwang [d]

[a] Max-Planck-Institut für Eisenforschung GmbH, Max-Planck-Str. 1, 40237, Düsseldorf, Germany
[b] Department of Materials Science and Engineering, Chungnam National University, Daejeon, 305-764, Republic of Korea
[c] Department of Materials Science and Engineering, Yonsei University, Seoul, 120-749, Republic of Korea
[d] Department of Materials Science and Engineering, Seoul National University of Science and Technology, Seoul, 139-743, Republic of Korea

ARTICLE INFO

Article history:
Received 12 August 2016
Received in revised form
23 September 2016
Accepted 27 September 2016
Available online 5 October 2016

Keywords:
Charpy impact test
Toughness
Ultrafine-grained materials
Intercritical annealing
Medium Mn steel
Brittle-ductile transition

ABSTRACT

The effects of prior austenite (γ) grain boundaries and microstructural morphology on the impact toughness of an annealed Fe-7Mn-0.1C-0.5Si medium Mn steel were investigated for two different microstructure states, namely, hot-rolled and annealed (HRA) specimens and cold-rolled and annealed (CRA) specimens. Both types of specimens had a dual-phase microstructure consisting of retained austenite (γ_R) and ferrite (α) after intercritical annealing at 640 °C for 30 min. The phase fractions and the chemical composition of γ_R were almost identical in both types of specimens. However, their microstructural morphology was different. The HRA specimens had lath-shaped morphology and the CRA specimens had globular-shaped morphology. We find that both types of specimens showed transition in fracture mode from ductile and partly quasi-cleavage fracture to intergranular fracture with decreasing impact test temperature from room temperature to −196 °C. The HRA specimen had higher ductile to brittle transition temperature and lower low-temperature impact toughness compared to the CRA specimen. This was due to intergranular cracking in the HRA specimens along prior γ grain boundaries decorated by C, Mn and P. In the CRA specimen intergranular cracking occurred along the boundaries of the very fine α and α' martensite grains. The results reveal that cold working prior to intercritical annealing promotes the elimination of the solute-decorated boundaries of coarse prior γ grains through the recrystallization of α' martensite prior to reverse transformation, hence improving the low-temperature impact toughness of medium Mn steel.

1. Introduction

During the last decades, advanced high strength steels with remarkable low-temperature toughness have been extensively studied for cryogenic applications, such as cryogenic offshore structures and storage tanks for liquefied natural gas [1–6]. Although Fe-Ni martensitic steel has been widely used for cryogenic applications due to its excellent strength and low-temperature toughness, the high price of Ni shifts attention to less expensive alloys [1–6]. In this regard, Fe-Mn martensitic steels with 3–10 wt% Mn, referred to as medium Mn steels [7–14], have received significant attention since both, Fe-Ni and Fe-Mn alloys are capable of producing similar types of lath martensitic microstructure and room-temperature mechanical properties [15–19]. However, medium Mn steels exhibit lower low-temperature toughness and higher ductile to brittle transition temperature (DBTT) compared to Fe-Ni martensitic steel. For example, Fe-9Ni and Fe-8Mn (wt%) steels show a DBTT of −77 °C and −20 °C and impact energies at −196 °C of 11 J and less than 1 J, respectively [19]. The high DBTT and poor low-temperature toughness of medium Mn steels are known to be due to severe intergranular fracture [15,16,20].

Recently, several studies reported that retained austenite (γ_R), when prevalent after reversion treatment from α' martensite to γ

* Corresponding author.
** Corresponding author.
E-mail addresses: d.ponge@mpie.de (D. Ponge), yklee@yonsei.ac.kr (Y.-K. Lee).

http://dx.doi.org/10.1016/j.actamat.2016.09.048
1359-6454/

austenite [21,22], is effective in improving the low-temperature toughness of medium Mn steel [20,23–25]. Hu et al. [23] compared the impact toughness of hot-rolled and annealed Fe-5Mn-0.04C (wt%) steels with and without the presence of γ_R. While specimens, annealed at 600 °C for 10 min, showed no γ_R, samples that were annealed at 650 °C for 10 min, contained γ_R with a volume fraction of ~0.15. The impact toughness of the steel containing γ_R was approximately ten times higher than that of corresponding samples without the presence of γ_R at test temperatures between −20 °C and 20 °C. This difference was attributed to the fact that metastable γ_R has high resistance to crack propagation. Similar results were also reported by Wang et al. [25]. Hu et al. [23] speculated that the γ, when reverted at the α' martensite grain boundaries, improves interface cohesion because it promotes Mn partitioning into the newly formed γ, hence reducing the segregation of Mn to grain boundaries [20]. Indeed segregation of Mn is known to deteriorate cohesion of grain boundaries in martensitic steels [18].

Kuzmina et al. [20] reported a change in impact toughness of hot-rolled and annealed Fe-9Mn (wt%) steel as a function of both, annealing temperature (450 °C and 600 °C) and time (10 s–860 h). When the annealing time was short (e.g. 10 s) at 450 °C, the Mn segregation at the prior γ grain boundaries of α' martensite substantially reduced the impact toughness. However, when the annealing time was long (e.g. 672 h) at 450 °C, reversion from α' martensite to γ at grain boundaries drastically reduced the grain boundary segregation of Mn via partitioning from α' into the newly formed γ phase, hence increasing the impact toughness. They also reported that B-containing Fe-9Mn (wt%) steel exhibited higher impact toughness compared to B-free Fe-9Mn (wt%) steel. This was attributed to the fact that B rapidly segregates with fast kinetics to pre-occupy the grain boundaries, and hence blocked the segregation of slowly diffusing Mn to the grain boundaries.

In contrast to these studies, Chen et al. [24] reported that hot-rolled and annealed Fe-5.1Mn-0.04C-1.4Ni (wt%) steel with a high volume fraction of γ_R (~0.14) showed a lower impact toughness at test temperatures between −100 °C and 20 °C compared to similar material with a lower volume fraction of γ_R (~0.10). This was attributed to the circumstance that the specimen with higher γ_R volume fraction had a lower mechanical stability of γ_R with lower C, Mn and Ni concentrations. While the chemical composition of γ_R in the steel with lower γ_R volume fraction was ~0.12C, ~10.41Mn and ~2.91Ni (in wt%), that of γ_R in the steel with higher γ_R volume fraction was ~0.07C, ~7.69Mn and ~2.29Ni (in wt%).

Although some of these previous studies on the impact toughness of medium Mn steels hence provided certain insights into the influence of volume fraction and phase stability of γ_R on the resulting impact toughness, the relationship between the underlying microstructural morphology and the toughness was not considered so far. The microstructural morphology of annealed medium Mn steels is known to change from a lath shape to a globular shape by cold rolling prior to intercritical annealing [9,14]. When the hot-rolled steel is intercritically annealed, the reverse transformation from α' martensite to γ occurs mainly along the martensite block boundaries prior to the recrystallization of α' martensite, resulting in lath-shaped grain morphology [9,10]. The absence of recrystallization of the α' martensite matrix partly leads to the prevalence of martensitic boundaries (e.g. the boundaries of prior γ grains, packets, blocks and laths) even after intercritical annealing [26]. However, when the cold-rolled steel is annealed, recrystallization of the α' martensite matrix and reverse transformation from α' martensite to γ can occur simultaneously due to the high dislocation density introduced by cold rolling, resulting in a globular-shaped grain morphology [9].

Therefore, in this study we prepared medium Mn steel specimens with two different microstructural morphologies, namely, lath and globular, but with similar volume fraction and chemical composition of the reversed austenite γ_R. Using the specimens, we investigated the relationship between microstructural morphology and impact toughness at various temperatures to derive a novel pathway to the microstructural design of medium Mn steels for improving their low-temperature toughness which takes microstructure morphology into account.

2. Experimental procedure

Details of synthesis and processing of the materials used are given in Ref. [26]: A 30 kg ingot of Fe-7Mn-0.1C-0.5Si (wt%) steel was prepared using a vacuum induction furnace. The chemical composition of the ingot was Fe-7.22Mn-0.093C-0.49Si-0.013Al-0.005P-0.007S (wt%). The ingot was homogenized at 1150 °C for 12 h in an Ar atmosphere, hot-rolled to a ~5.5-mm thick plate at temperatures ranging from ~1100 °C to 900 °C, and then air-cooled to room temperature. The hot-rolled specimen showed a single α' martensite phase without γ_R. The average size of the prior γ grains was ~35 μm [26]. Here, γ refers to the original high-temperature austenite formed prior to air cooling and its grain boundaries are inherited to the as-cooled martensite structure. A part of the hot-rolled plate was cold-rolled to ~2.0-mm thick sheets with a thickness reduction of ~55% after surface descaling.

Both the hot-rolled and cold-rolled specimens were intercritically annealed at 640 °C for 30 min using a vacuum tube furnace, and then water-quenched to room temperature. The annealing temperature was in between the equilibrium eutectoid (A_{e1}) and ferrite start (A_{e3}) temperatures. Both A_{e1} and A_{e3} temperatures were calculated using Thermo-Calc software in conjunction with the TCFE7 database. Hereafter, the hot-rolled plus annealed types of specimens are referred to as 'HRA' specimens and the cold-rolled plus annealed ones are referred to as 'CRA' specimens.

Microstructures of both, HRA and CRA materials were probed using a field-emission scanning electron microscope (FE-SEM; JEOL, JSM-6500F) equipped with an electron backscattered diffractometer (EBSD; EDAX-TSL, Digiview-IV). Specimens for EBSD were polished using a suspension of 0.04 μm colloidal silica particles, and electro-polished in a mixed solution of 90% glacial acetic acid (CH_3COOH) and 10% perchloric acid ($HClO_4$) at ~15 V for 60 s to remove the layers damaged by mechanical polishing. The acceleration voltage, probe current, working distance and step size for EBSD operation were 15 kV, 12 nA, 15 mm and 30 nm, respectively.

The phase fraction in the specimens was measured using a high-resolution X-ray diffractometer (XRD; RIGAKU, SmartLab) and Cu-$K_{\alpha 1}$ radiation (λ = 1.5405 Å). Specimens for XRD characterization were electro-polished using the same solution used as for EBSD sample preparation. The scanning range, rate and step size were 40°–100°, 2° min^{-1} and 0.02°, respectively. The volume fraction of γ_R was calculated using the integrated intensities of all diffracted peaks [27].

To investigate solute segregation at grain boundaries [28,29] in as-hot-rolled specimens, atom probe tomography (APT) was conducted using a local electrode atom probe detector (Imago Scientific Instruments, LEAP 5000X HR™) [30–35]. APT was performed at a base temperature of ~50 K in laser-pulsed mode at 30 pJ pulse energy. The wavelength, pulse rate and detection rate of the laser were 355 nm, 500 kHz and 1.5%, respectively. The needle-shaped APT specimens were prepared using a dual-focused ion beam microscope (FIB; FEI Helios, Nano-Lab600i) [36,37]. Specimens were mounted on the top of standard Si micro-tips, and sharpened by annular ion milling. Data analysis for atomic reconstructions was conducted using the IVAS® software provided by Imago Scientific Instruments [30–35].

The sub-sized Charpy 45° V-notch specimens (ASTM E23) of both hot-rolled and cold-rolled steels were machined along the rolling direction. The dimension of the specimens was ~2.0 mm in thickness, ~10 mm in width and 55 mm in length. Charpy impact tests were performed at temperatures ranging from −196 °C to 50 °C. The temperature of the specimens was controlled using water and a hot plate for elevated-temperature tests and iso-pentane and liquid nitrogen for the sub-room temperature tests. Testing temperatures were monitored by a K-type thermocouple. Impact testing was for each temperature performed at least on three separate specimens.

3. Results and discussion

Fig. 1 shows EBSD image quality (IQ)-phase maps of the HRA and CRA specimens. Both intercritically annealed specimens have a dual-phase microstructure of α ferrite and retained austenite γ_R[26]. The phases colored in red and green correspond to α and γ_R, respectively. The blue and black lines represent low-angle boundaries with misorientation angles below 15° and high-angle boundaries with misorientation angles above 15°, respectively. The HRA specimen has lath-shaped α (abbreviated as α_L) and γ_R (abbreviated as γ_L) grains due to the absence of recrystallization of the α′ martensite matrix prior to reverse transformation. The average sizes of the α_L and γ_L grains are ~300 nm and 260 nm, respectively (Fig. 1a). The volume fraction of γ_L was measured to be ~0.47 using XRD [26], and the average concentrations of Mn and C in γ_L were ~10.3 ± 0.7 wt% and ~0.22 ± 0.03 wt%, respectively. The Mn concentration was measured using TEM-EDXS. The C concentration was calculated using a composition sensitive phenomenological equation for the lattice parameter of γ as outlined in Ref. [26].

The CRA specimen has globular-shaped α (abbreviated as α_G) and γ_R (abbreviated as γ_G) grains due to primary recrystallization of the α′ martensite matrix prior to reverse transformation. The average in-plane diameters of the α_G and γ_G grains are both ~450 nm (Fig. 1b). The volume fraction of γ_G (~0.50) was slightly higher than that of γ_L (~0.47) [26] because cold-rolling accelerated the reverse transformation from α′ martensite to γ. The average concentrations of Mn and C in γ_G were ~10.1 ± 0.5 wt% and ~0.20 ± 0.02 wt%, respectively [26].

Fig. 2 shows the variation of the Charpy impact energy values for the HRA and CRA specimens tested at temperatures in the range between −195 °C and 50 °C. The HRA specimen showed slightly higher impact energies above room temperature than the CRA specimen. Both specimens showed a drop in the impact energy with decreasing test temperature from 0 °C to −100 °C. This applied particularly to the HRA specimens. Accordingly, the HRA specimens possessed lower impact energy at low temperatures of ≤ −50 °C compared to the CRA specimens, and also showed higher DBTT of ~ −50 °C relative to the CRA specimens (~−75 °C). The DBTT was determined as a temperature corresponding to the half of the sum of the upper shelf energy (the average value of impact energies measured above room temperature) and the lower shelf energy (the average value of impact energies measured at temperatures of below −100 °C) [20].

For investigating the reason for the difference in impact toughness between the HRA and CRA specimens which was observed irrespective of the fact that they have similar volume fractions and chemical composition of γ_R, XRD analysis of both specimens was performed before and after the Charpy impact tests at 25 °C and −196 °C (Fig. 3). The measured XRD volume fractions of γ_R in each specimen are listed in Table 1. After impact testing, the CRA specimens showed a higher amount of transformed γ_R compared to the HRA specimens, regardless of the test temperature (Table 1). However, the volume fraction of γ_R which was transformed during quenching from room temperature to −196 °C was 0.15–0.17, which was similar in both types of specimens. This result suggests that the HRA specimens had higher mechanical stability of their γ_R phase content compared to the CRA specimens, although the thermal stability of γ_R was almost similar in both specimens. Considering the fact that both, γ_L and γ_G had almost identical concentrations of Mn and C, their shape and size was probably related to the mechanical stability of γ_R. More specific, the data indicate that a higher shear stress was required for the martensitic transformation of the γ_L phase with a narrow width of ~260 nm,

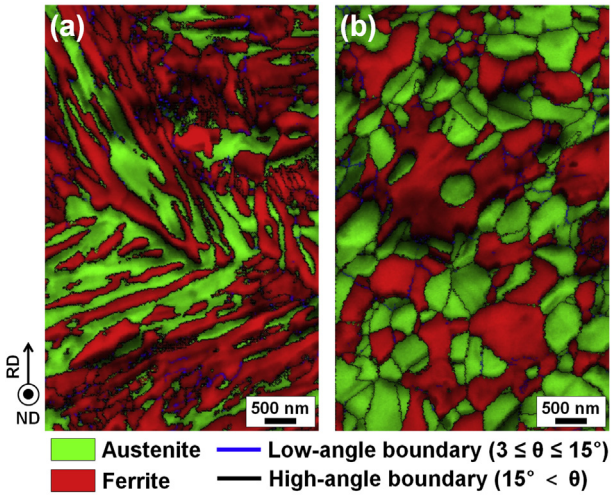

Fig. 1. EBSD IQ-phase maps taken from the normal direction of (a) the hot-rolled and annealed (HRA) specimen and (b) the cold-rolled and annealed (CRA) specimen. Austenite is in green. Ferrite is in red. The blue lines are low-angle bounsdaries with misorientation angles of 3°–15°. The black lines are high-angle boundaries with misorientation angles of over 15°. IQ: image quality. (For interpretation of the references to colour in this figure legend, the reader is referred to the web version of this article.)

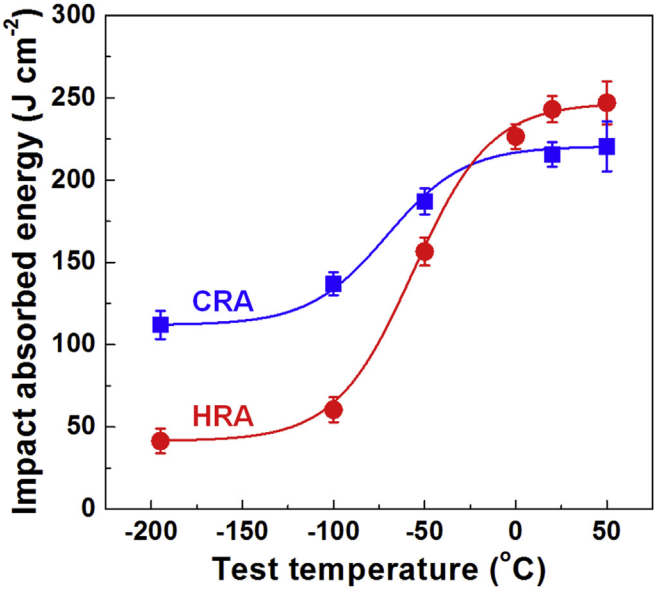

Fig. 2. Charpy impact absorbed energy vs. impact test temperature curves of both, the hot-rolled and annealed (HRA) specimen and the cold-rolled and annealed (CRA) specimen.

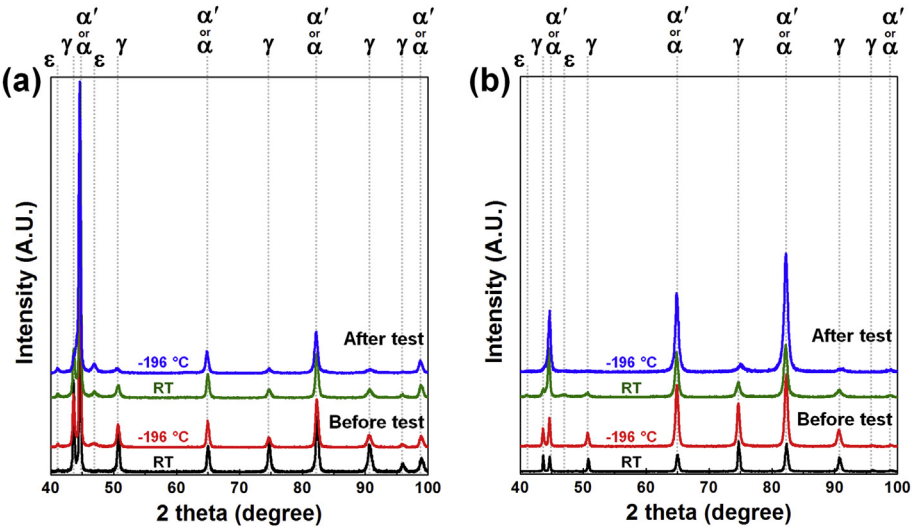

Fig. 3. XRD patterns of (a) the hot-rolled and annealed (HRA) specimen and (b) the cold-rolled and annealed (CRA) specimen before and after Charpy impact tests at 25 °C and −196 °C.

Table 1
Change in volume fraction of retained austenite, measured by XRD analysis, in hot-rolled and annealed (HRA) specimens and in cold-rolled and annealed (CRA) specimen before and after Charpy impact testing at 25 °C and −196 °C.

Impact test temperature	HRA specimen		CRA specimen	
	Before test	After test	Before test	After test
25 °C	0.47	0.25	0.50	0.20
−196 °C	0.32	0.14	0.33	0.09

compared to the γ_G phase fraction with a diameter of ~450 nm. This phenomenon was considered to be relevant, particularly for strain-induced martensitic transformation of such variants with a favorable orientation relationship between the tensile axis and the grain orientation of γ_R. Therefore, the reason for the slightly higher upper shelf energy of the HRA specimens relative to the CRA material (Fig. 2) was the slightly higher mechanical stability of γ_R in the HRA specimens.

However, since the difference in low-temperature toughness between the HRA and CRA specimens cannot be readily explained exclusively in terms of the difference in mechanical stability of their respective γ_R phase fractions, post-mortem microstructural analysis was additionally conducted using fractured specimens. Fig. 4 shows SEM fractographs of the HRA specimens taken from different test temperatures. The HRA specimen, which fractured at room temperature (Fig. 4a), showed mainly a ductile-fractured surface with fine dimples. Some portions of the fracture surface exhibited quasi-cleavage appearance caused by rapid crack propagation through strain-induced α′ martensite [38]. When fractured at −50 °C (Fig. 4b–d), i.e. near the DBTT, the fracture surface of the HRA specimen revealed a mixed fracture mode containing ductile fracture portions featuring fine dimples (Fig. 4c) and brittle fracture zones characterized by quasi-cleavage (Fig. 4b) and intergranular fracture (Fig. 4d). The detached boundaries of intergranularly fractured grains show both rugged facets and flat facets, and the size of the fractured grains (~36 μm) was similar to the size of prior γ grains (~35 μm) [26]. This implies that intergranular fracture along the boundaries of prior γ grains operated partially at −50 °C. The HRA specimen, which was fractured at −196 °C, showed prevalent intergranular fracture without fine dimples and without quasi-cleavage features (Fig. 4e and f). This result suggests that the fracture mode of the HRA specimens changed from a mixed fracture mode of ductile fracture plus quasi-cleavage brittle fracture to intergranular fracture occurring along the boundaries of prior γ grains with decreasing impact test temperature.

To reconfirm the intergranular fracture, the surface of the HRA specimen, which was fractured at −196 °C, was observed from a normal direction using EBSD (Fig. 5). The white lines in the EBSD IQ-inverse pole figure (IPF) map are the grain boundaries of the prior γ grains. The boundaries are highlighted by misorientation angles of 20°–50° in *bcc* phase [20] using TSL-OIM software and retouched by image analyzer for effective visualization. The EBSD IQ-IPF map clearly reveals that a crack had propagated along the boundaries of the prior γ grains (Fig. 5a), hence confirming intergranular fracture. For detailed analysis, the region around the crack (dotted yellow box in Fig. 5a) was enlarged and probed at higher resolution. The upper part shows the flat surface and the lower part exhibits the rugged surface (Fig. 5b). While the flat surface is parallel to the elongated γ_L grains, the rugged surface describes a certain angle relative to the elongated γ_L grains. This observation indicates that the surface characteristics are determined by the angle between the crack propagating along the boundaries of the prior γ grains and the elongated γ_L grains.

Yet, it remains still unclear why the intergranular fracture occurred mainly along the boundaries of the prior γ grains in the HRA specimen instead of propagating along other high angle boundaries such as along the martensitic packet or block boundaries. This effect can be discussed based on previous reports which showed that the boundaries of prior γ grains can carry more segregation of alloying elements and impurities than the boundaries of martensitic packets and blocks [22] and the fact that such segregation deteriorates interface cohesion [20]. To confirm the difference in the degree of segregation pertaining to a certain type of interfaces, APT analysis was conducted on an as-hot-rolled specimen which was air-cooled to room temperature (Fig. 6). The APT tip was prepared using the site-specific FIB lift-out technique [20,30–35,39]. The needle-shaped APT sample was cut out and milled at a location containing boundaries of prior γ grains. The location for tip extraction was identified by SEM and EBSD analysis (Fig. 6a). Fig. 6b shows the three-dimensional APT result. C isosurfaces with a concentration of ~2 at.% are plotted to highlight the decorated grain boundaries (GB1 and GB2). The C segregation to

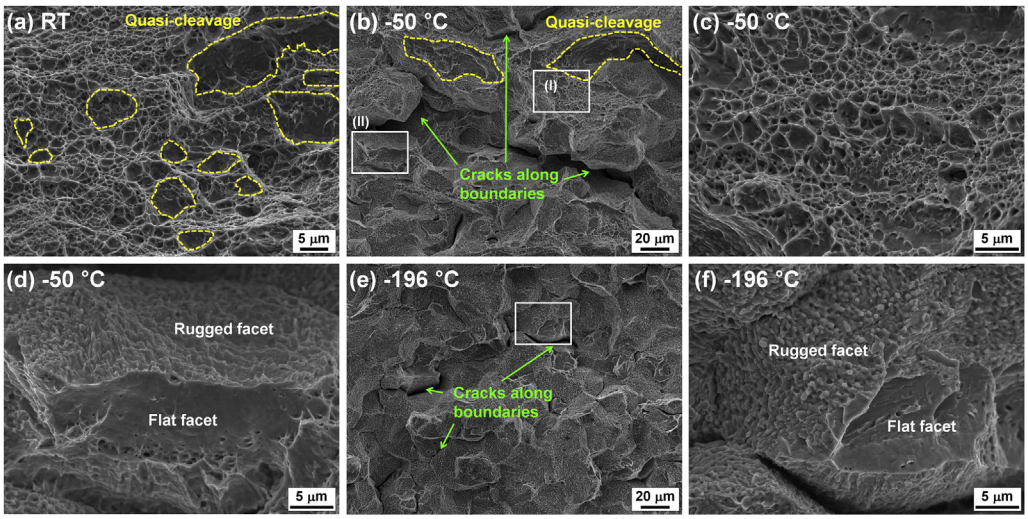

Fig. 4. SEM fractographs of the hot-rolled and annealed (HRA) specimen fractured at (a) room temperature, (b, c, d) −50 °C and (e, f) −196 °C. (c) and (d) highly magnified images taken at the region marked by the white boxes of (I) and (II) in (b), respectively, and (f) a highly magnified image taken at the region marked by the white box in (e).

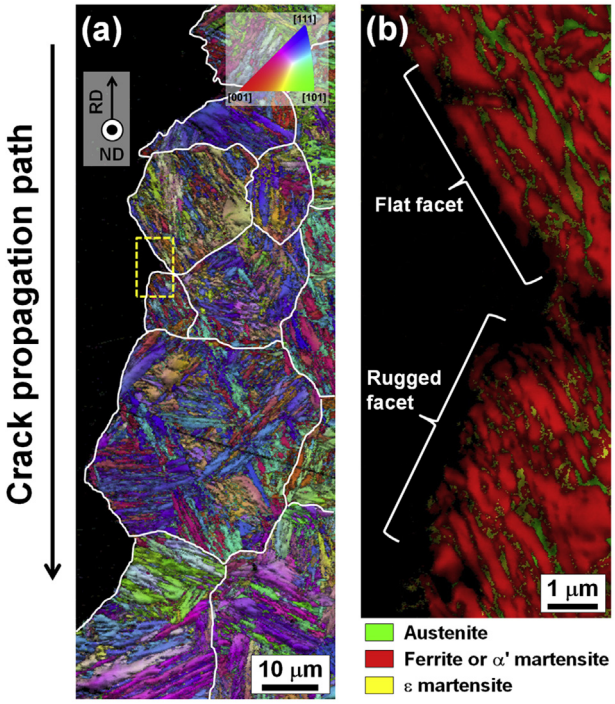

Fig. 5. (a) EBSD IQ-IPF map taken from the normal direction of the hot-rolled and annealed (HRA) specimen fractured at −196 °C and (b) EBSD IQ-phase map taken at the region marked by the yellow box in (a). IQ: image quality; IPF: inverse pole figure. (For interpretation of the references to colour in this figure legend, the reader is referred to the web version of this article.)

the boundaries is assumed to occur primarily during air cooling at temperatures of below the martensite start (M_s) temperature due to the high mobility of the C atoms [20,39]. The M_s temperature of the present steel was calculated as ~275 °C using Mahieu's equation [40].

Fig. 6c shows the one-dimensional elemental profiles corresponding to interfaces GB1 and GB2. While GB1 revealed only C segregation, GB2 was decorated by C, Mn and P. Both Mn and P are known as harmful elements reducing grain boundary cohesion [20]. As substitutional Mn and P atoms cannot diffuse sufficiently far below the M_s temperature, both elements must have segregated to the boundaries already in the single phase γ region at high temperatures above M_s. This observation indicates that GB2 is a prior γ grain boundary and GB1 is a boundary pertaining to martensite packets or blocks which formed at low temperatures below the M_s temperature. This result is in good agreement with previous atom probe observations reported by Morsdorf et al. [41] and Hutchinson et al. [42]. Thus we can confirm that the segregation of Mn and P atoms at the prior γ grain boundaries indeed deteriorate interface cohesion, promoting intergranular cracking at low temperatures below ~−50 °C.

Fig. 7 shows the surfaces of CRA specimens fractured at different temperatures. Like observed for the HRA sample, the CRA specimen, which was fractured at room temperature (Fig. 7a), had a large ductile-fractured region with fine dimples and a small brittle-fractured region featuring quasi-cleavage zones. When the CRA specimen was fractured at −100 °C (Fig. 7b–d), i.e. below the DBTT (−75 °C), it still revealed fine dimples (white arrows in Fig. 7c) and quasi-cleavage features (yellow dashed lines in Fig. 7b and c). In addition, intergranular fracture (green arrows in Fig. 7c and d) was also observed. When the CRA specimen was fractured at −196 °C, it exhibited only intergranular fracture without fine dimples and quasi-cleavage features (Fig. 7e and f). The average size of intergranularly fractured grains (green arrows in Fig. 7c and d) was ~500 nm, which is similar to the average size of both the α_G and γ_G grains (~450 nm) (Fig. 1b). This result suggests that the fracture mode of the CRA material changed from ductile and partly quasi-cleavage fracture to intergranular fracture with decreasing impact test temperature from room temperature to −196 °C.

To examine the mechanism of intergranular cracking at low temperature, the surface of the CRA specimen, which was fractured at −196 °C, was observed from a normal perspective using EBSD (Fig. 8). The dark gray grains in the EBSD IQ map (Fig. 8a) were interpreted as thermally-induced or strain-induced α′ martensite grains, since the EBSD signals indicated a *bcc* lattice structure with low confidence index (CI) values due to significant lattice distortion (Fig. 8b). The EBSD maps revealed that the crack, initiated from the V-notch of the specimen, had primarily propagated along the boundaries of both the α_G and α′ martensite grains and that there were few γ_G grains at the fractured surface. This result indicates that the γ_G grains near the crack were exposed to high stress concentrations and thus transformed to α′ martensite. The

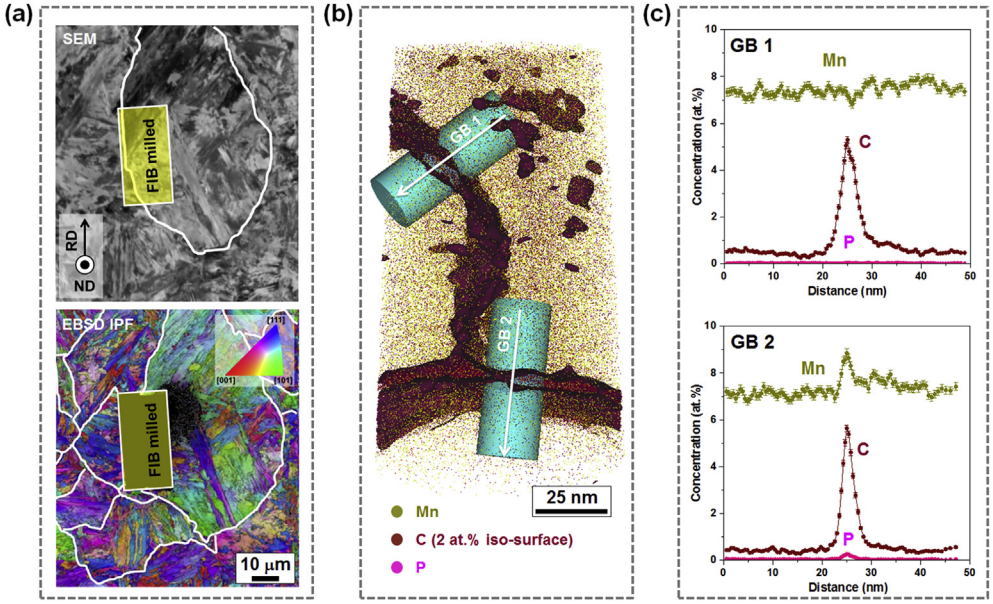

Fig. 6. (a) SEM and EBSD IQ-IPF maps taken from the normal direction of the as-hot-rolled specimen which was air-cooled to room temperature showing the boundaries of prior γ grains in terms of white lines. (b) Three-dimensional APT result of a needle-shaped specimen containing two grain boundaries. The needle-shaped specimen was milled at the region marked by the yellow box in Fig. 6a, and the C iso-surface with the concentration of 2 at.% was used to highlight the decoration of the grain boundaries. (c) One-dimensional element profiles obtained by scanning grain boundaries in Fig. 6b. IQ: image quality; IPF: inverse pole figure; APT: atom probe tomography. (For interpretation of the references to colour in this figure legend, the reader is referred to the web version of this article.)

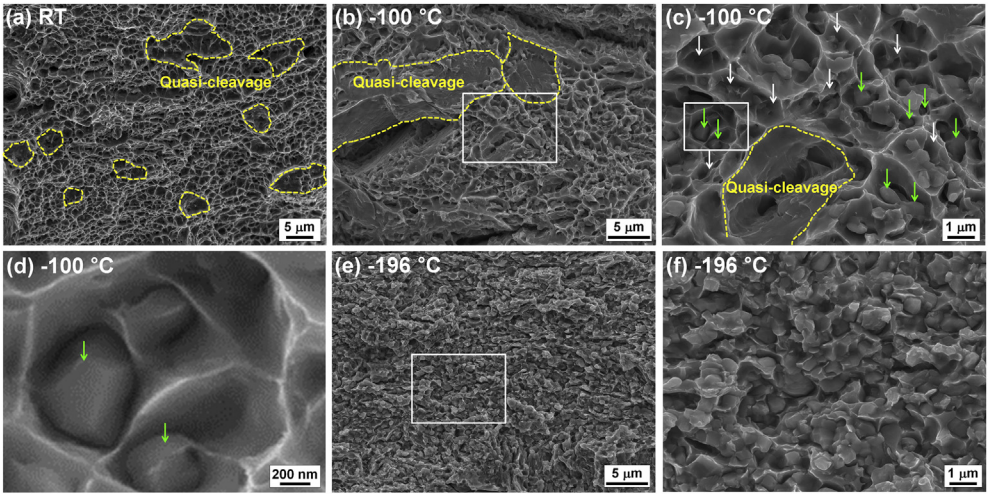

Fig. 7. SEM fractographs of the cold-rolled and annealed (CRA) specimen fractured at (a) room temperature, (b, c, d) −100 °C and (e, f) −196 °C. (c) a highly magnified image taken at the region marked by the white box in (b), (d) a highly magnified image taken at the region marked by the white box in (c), and (f) a highly magnified image taken at the region marked by the white box in (e).

intergranular crack was hence proceeding along the boundaries of α_G, thermally-induced α′ martensite and strain-induced α′ martensite grains. The intergranular cracking occurring along the boundaries of fine α_G and α′ grains in the CRA specimen is quite different from that propagating along prior γ grain boundaries decorated with Mn and P observed in the HRA specimen (Fig. 9). This difference in intergranular cracking behavior and low-temperature toughness can be fully attributed to the underlying different microstructural morphologies of the two types of specimens. It is remarkable that such profound differences arise even for two types of microstructures that can both be readily obtained for a medium Mn steel with identical chemical composition.

From the impact tests and post-mortem microstructural analysis, we conclude that the weakest feature in the microstructure is the prior γ grain boundaries. In the HRA samples, the grain boundary segregation content is inherited from the γ into the martensitic state and even the γ reversion treatment in conjunction with the associated elemental partitioning is not sufficient to significantly improve the cohesion of these solute decorated weak prior γ grain boundaries. However, in contrast to quenched and tempered medium carbon steels, most medium Mn steels can be subjected to cold rolling for a range of alloy compositions. In combination with a subsequent intercritical annealing treatment it is thus possible by primary recrystallization, i.e. a reconstructive mechanism, of the deformed martensite to completely sweep and hence eliminate these weak prior γ grain boundaries. The

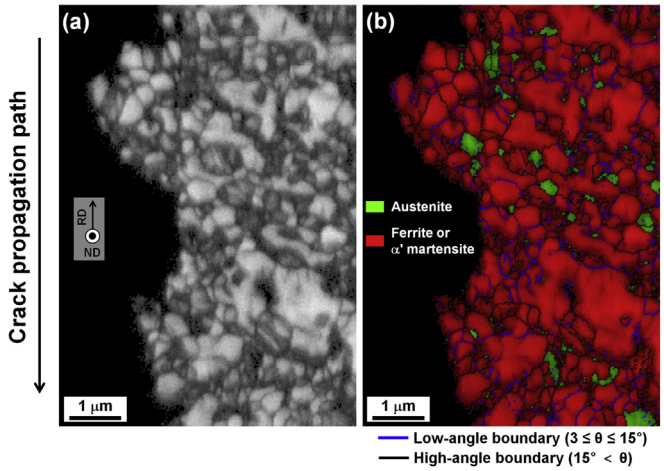

Fig. 8. (a) EBSD IQ map and (b) EBSD IQ-phase map taken from the normal direction of the cold-rolled and annealed (CRA) specimen fractured at −196 °C. In the phase map, austenite is in green, ferrite is in red. The blue lines are low-angle boundaries with misorientation angles of 3°–15°, and the black lines indicate high-angle boundaries with misorientation angles of over 15°. IQ: image quality. (For interpretation of the references to colour in this figure legend, the reader is referred to the web version of this article.)

corresponding improvement is clearly visible from our results, especially the increased lower shelf energy for the CRA sample and the reduced DBTT. Therefore, we suggest that appropriate cold working or warm working, leading to enhanced dislocation density storage, should be performed prior to intercritical annealing of medium Mn steels for promoting recrystallization of the α′ martensite matrix. Such a straightforward procedure is expected to eliminate the inherited weak prior γ grain boundaries and thus improve the impact toughness of medium Mn steels at low temperatures.

4. Conclusions

We studied the effects of prior austenite (γ) grain boundaries and microstructural morphology on the impact toughness of an annealed Fe-7Mn-0.1C-0.5Si (wt%) medium Mn steel. Two types of microstructures were produced, one type via hot-rolling plus annealing (HRA) and another one by cold-rolling plus annealing (CRA). Both types of specimens had a dual-phase microstructure consisting of retained austenite (γ) and ferrite (α) after intercritical annealing.

(1) Both, the HRA and CRA specimens were characterized by a transition in fracture mode from ductile and partly quasi-cleavage fracture to intergranular fracture with decreasing impact test temperature from room temperature to −196 °C.
(2) The HRA specimens exhibited a higher ductile to brittle transition temperature (DBTT) and lower impact energy at low temperatures below −50 °C compared to the CRA specimens; e.g. the DBTT of HRA and CRA specimens was ~−50 °C and ~−75 °C, and the impact energy at −195 °C of them was ~40 J cm^{-2} and ~120 J cm^{-2}, respectively. Both types of specimens failed by intergranular cracking. The intergranular cracks in HRA specimens propagated primarily along the boundaries of the prior austenite grains with a size of ~35 μm, but those in the CRA material propagated along the boundaries of the ferrite and α′ martensite grains with a much finer size of ~450 nm.
(3) The main reason for intergranular cracking along the prior austenite grains in the HRA specimen was the segregation of Mn and P at the grain boundaries occurring during homogenization, hot rolling and air-cooling prior to intercritical annealing. The boundaries of martensitic packets or blocks were decorated only by C, since substitutional diffusion of Mn and P towards the grain boundaries at low temperature below the M_s temperature of ~275 °C was too slow.

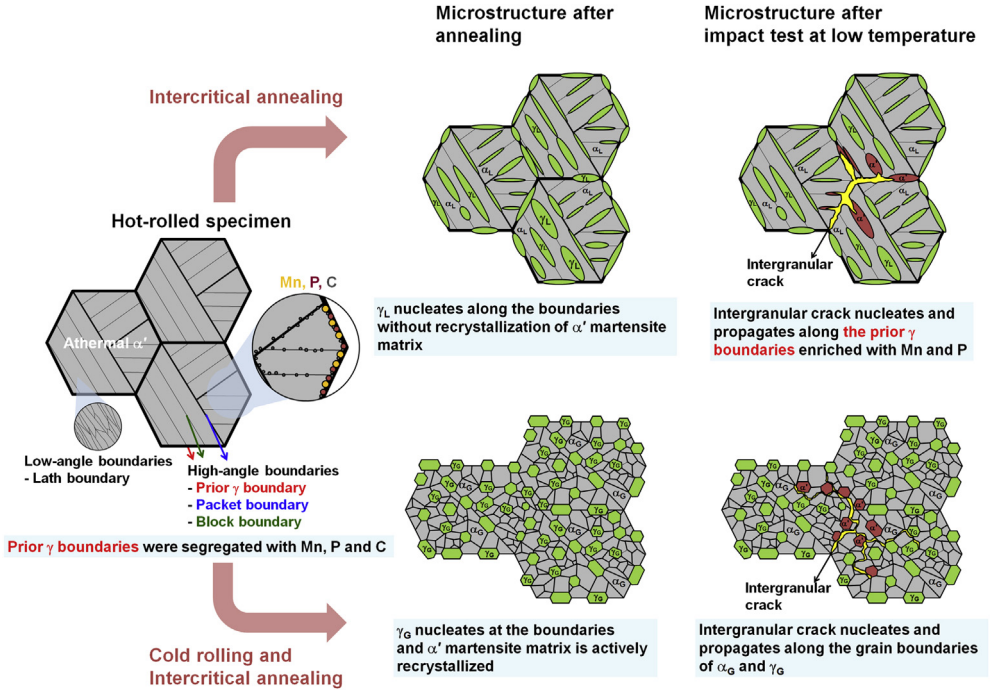

Fig. 9. Schematic sketch showing the difference in intergranular cracking occurring during the low-temperature impact test in two types of specimens with different microstructural morphologies after annealing. γ is reverted austenite, γ_L is lath-shaped retained austenite, γ_G is globular-shaped retained austenite, α′ is martensite, α_L is lath-shaped ferrite and α_G is globular-shaped ferrite.

(4) Cold or warm working prior to intercritical annealing of medium Mn steels promotes primary recrystallization of their formable α' martensite matrix prior to reverse transformation so that the solute-segregated boundaries of coarse prior austenite grains can be eliminated. We refer to this effect as 'prior austenite grain boundary break-up' mechanism. It results in the improvement of the low-temperature impact toughness of medium Mn steels.

Acknowledgements

Jeongho Han is grateful to the kind support of the Alexander von Humboldt Stiftung (AvH, Alexander von Humboldt Foundation, https://www.humboldt-foundation.de). Alisson Kwiatkowski da Silva is grateful to the Brazilian National Research Council (Conselho Nacional de Pesquisas, CNPQ) for the Ph.D. scholarship through the "Science without Borders" Project.

References

[1] I. Watanabe, M. Suzuki, Y. Matsuda, H. Tagawa, K. Matsui, S. Shimada, Fracture toughness of 9% Ni steel and safety of LNG storage tank against brittle fracture, Nippon. Kokan Tech. Rep. 42 (1984) 2–10.
[2] H. Tagawa, K. Matsui, T. Izawa, I. Watanabe, M. Suzuki, T. Tokunaga, Nine-percent Ni steel plates manufactured by the direct-quenching and tempering process, Nippon. Kokan Tech. Rep. 46 (1986) 112–119.
[3] N. Saitoh, H. Muraoka, R. Yamaba, O. Saeki, Development of heavy 9% nickel steel plates with superior low-temperature toughness for LNG storage tanks, Nippon. Steel Tech. Rep. 58 (1993) 9–16.
[4] M. Hoshino, N. Saitoh, H. Muraoka, O. Saeki, Development of super-9%Ni steel plates with superior low-temperature toughness for LNG storage tanks, Nippon. Steel Tech. Rep. 90 (2004) 20–24.
[5] N. Nakada, J. Syarif, T. Tsuchiyama, S. Takaki, Improvement of strength–ductility balance by copper addition in 9%Ni steels, Mater. Sci. Eng. A 374 (2004) 137–144.
[6] X.Q. Zhao, T. Pan, Q.F. Wang, H. Su, C.F. Yang, Q.X. Yang, Y.Q. Zhang, Effect of intercritical quenching on reversed austenite formation and cryogenic toughness in QLT-processed 9% Ni steel, J. Iron. Steel Res. Int. 14 (2007) 240–244.
[7] Y.-K. Lee, J. Han, Current opinion in medium manganese steel, Mater. Sci. Technol. 31 (2015) 843–856.
[8] J. Han, Y.-K. Lee, The effects of the heating rate on the reverse transformation mechanism and the phase stability of reverted austenite in medium Mn steels, Acta Mater. 67 (2014) 354–361.
[9] J. Han, S.-J. Lee, J.-G. Jung, Y.-K. Lee, The effects of the initial martensite microstructure on the microstructure and tensile properties of intercritically annealed Fe–9Mn–0.05 C steel, Acta Mater. 78 (2014) 369–377.
[10] M. Calcagnotto, D. Ponge, E. Demir, D. Raabe, Orientation gradients and geometrically necessary dislocations in ultrafine grained dual-phase steels studied by 2D and 3D EBSD, Mater. Sci. Eng. A 527 (2010) 2738–2746.
[11] S. Lee, S.J. Lee, S. Santhosh Kumar, K. Lee, B.C.D. Cooman, Localized deformation in multiphase, ultra-fine-grained 6 Pct Mn transformation-induced plasticity steel, Metall. Mater. Trans. A 42 (2011) 3638–3651.
[12] H. Luo, J. Shi, C. Wang, W. Cao, X. Sun, H. Dong, Experimental and numerical analysis on formation of stable austenite during the intercritical annealing of 5Mn steel, Acta Mater. 59 (2011) 4002–4014.
[13] C. Wang, J. Shi, C.Y. Wang, W.J. Hui, M.Q. Wang, H. Dong, W.Q. Cao, Development of ultrafine lamellar ferrite and austenite duplex structure in 0.2C5Mn steel during ART-annealing, ISIJ Int. 51 (2011) 651–656.
[14] M.M. Wang, C.C. Tasan, D. Ponge, D. Raabe, Spectral TRIP enables ductile 1.1 GPa martensite, Acta Mater. 111 (2016) 262–272.
[15] M.J. Roberts, Effect of transformation substructure on the strength and toughness of Fe-Mn alloys, Metall. Trans. 1 (1970) 3287–3294.
[16] B.C. Edwards, M. Nasim, E.A. Wilson, The nature of intergranular embrittlement in quenched Fe-Mn alloys, Scr. Metall. 12 (1978) 377–380.
[17] S.K. Hwang, J.W. Morris, The improvement of cryogenic mechanical properties of Fe-12 Mn and Fe-8 Mn alloy steels through thermal/mechanical treatments, Metall. Trans. A 10 (1979) 545–555.
[18] N.H. Heo, J.W. Nam, Y.U. Heo, S.J. Kim, Grain boundary embrittlement by Mn and eutectoid reaction in binary Fe-12Mn steel, Acta Mater. 61 (2013) 4022–4034.
[19] K.H. Kwon, I.C. Yi, Y. Ha, K.K. Um, J.K. Choi, K. Hono, K. Oh-ishi, N.J. Kim, Origin of intergranular fracture in martensitic 8Mn steel at cryogenic temperatures, Scr. Mater. 69 (2013) 420–423.
[20] M. Kuzmina, D. Ponge, D. Raabe, Grain boundary segregation engineering and austenite reversion turn embrittlement into toughness: example of a 9 wt% medium Mn steel, Acta Mater. 86 (2015) 182–192.
[21] M. Kuzmina, M. Herbig, D. Ponge, S. Sandlöbes, D. Raabe, Linear complexions: confined chemical and structural states at dislocations, Science 349 (2015) 1080–1083.
[22] O. Dmitrieva, D. Ponge, G. Inden, J. Millán, P. Choi, J. Sietsma, D. Raabe, Chemical gradients across phase boundaries between martensite and austenite in steel studied by atom probe tomography and simulation, Acta Mater. 59 (2011) 364–374.
[23] J. Hu, L.-X. Du, G.-S. Sun, H. Xie, R.D.K. Misra, The determining role of reversed austenite in enhancing toughness of a novel ultra-low carbon medium manganese high strength steel, Scr. Mater. 104 (2015) 87–90.
[24] J. Chen, M. Lv, S. Tang, Z. Liu, G. Wang, Correlation between mechanical properties and retained austenite characteristics in a low-carbon medium manganese alloyed steel plate, Mater. Charact. 106 (2015) 108–111.
[25] M.M. Wang, C.C. Tasan, D. Ponge, A.C. Dippel, D. Raabe, Nanolaminate transformation-induced plasticity–twinning-induced plasticity steel with dynamic strain partitioning and enhanced damage resistance, Acta Mater. 85 (2015) 216–228.
[26] J. Han, J.-H. Nam, Y.-K. Lee, The mechanism of hydrogen embrittlement in intercritically annealed medium Mn TRIP steel, Acta Mater. 113 (2016) 1–10.
[27] B.D. Cullity, S.R. Stock, Elements of X-ray Diffraction, Prentice hall, Inc., New Jersey, 2001.
[28] B.W. Krakauer, J.G. Hu, S.M. Kuo, R.L. Mallick, A. Seki, D.N. Seidman, J.P. Baker, R.J. Loyd, A system for systematically preparing atom-probe field-ion-microscope specimens for the study of internal interfaces, Rev. Sci. Instrum. 61 (1990) 3390–3398.
[29] Y. Toji, H. Matsuda, M. Herbig, P.-P. Choi, D. Raabe, Atomic-scale analysis of carbon partitioning between martensite and austenite by atom probe tomography and correlative transmission electron microscopy, Acta Mater. 65 (2014) 215–228.
[30] D. Raabe, S. Sandlöbes, J. Millán, D. Ponge, H. Assadi, M. Herbig, P.P. Choi, Segregation engineering enables nanoscale martensite to austenite phase transformation at grain boundaries: a pathway to ductile martensite, Acta Mater. 61 (2013) 6132–6152.
[31] D. Raabe, M. Herbig, S. Sandlöbes, Y. Li, D. Tytko, M. Kuzmina, D. Ponge, P.P. Choi, Grain boundary segregation engineering in metallic alloys: a pathway to the design of interfaces, Curr. Opin. Solid State Mater. Sci. 18 (2014) 253–261.
[32] B. Gault, M.P. Moody, J.M. Cairney, S.P. Ringer, Atom probe crystallography, Mater. Today 15 (2012) 378–386.
[33] V.J. Araullo-Peters, B. Gault, S.L. Shrestha, L. Yao, M.P. Moody, S.P. Ringer, J.M. Cairney, Atom probe crystallography: atomic-scale 3-D orientation mapping, Scr. Mater. 66 (2012) 907–910.
[34] M.P. Moody, F. Tang, B. Gault, S.P. Ringer, J.M. Cairney, Atom probe crystallography: characterization of grain boundary orientation relationships in nanocrystalline aluminium, Ultramicroscopy 111 (2011) 493–499.
[35] T.F. Kelly, D.J. Larson, Atom probe tomography 2012, Annu. Rev. Mater. Res. 42 (2012) 1–31.
[36] P.J. Felfer, T. Alam, S.P. Ringer, J.M. Cairney, A reproducible method for damage-free site-specific preparation of atom probe tips from interfaces, Microsc. Res. Tech. 75 (2012) 484–491.
[37] M. Herbig, D. Raabe, Y.J. Li, P. Choi, S. Zaefferer, S. Goto, Atomic-Scale quantification of grain boundary segregation in nanocrystalline material, Phys. Rev. Lett. 112 (2014) 126103.
[38] H. Asahi, D. Hirakami, S. Yamasaki, Hydrogen trapping behavior in vanadium-added steel, ISIJ Int. 43 (2003) 527–533.
[39] M. Herbig, M. Kuzmina, C. Haase, R.K.W. Marceau, I. Gutierrez-Urrutia, D. Haley, D.A. Molodov, P. Choi, D. Raabe, Grain boundary segregation in Fe–Mn–C twinning-induced plasticity steels studied by correlative electron backscatter diffraction and atom probe tomography, Acta Mater. 83 (2015) 37–47.
[40] S. Lee, B.C. De Cooman, On the selection of the optimal intercritical annealing temperature for medium Mn TRIP steel, Metall. Mater. Trans. A 44 (2013) 5018–5024.
[41] L. Morsdorf, C.C. Tasan, D. Ponge, D. Raabe, 3D structural and atomic-scale analysis of lath martensite: effect of the transformation sequence, Acta Mater. 95 (2015) 366–377.
[42] B. Hutchinson, J. Hagström, O. Karlsson, D. Lindell, M. Tornberg, F. Lindberg, M. Thuvander, Microstructures and hardness of as-quenched martensites (0.1–0.5%C), Acta Mater. 59 (2011) 5845–5858.